Oxidative synthesis of yellow photoluminescent carbon nanoribbons from carbon black

Saeed Khodabakhhshi,*[a] Pasquale F. Fulvio,[b] Ahmad Sousaraei,[c] Sajad Kiani,[a] Yubiao Niu,[d] Richard E. Palmer,[d] Winson C. H. Kuo,[e] Jennifer Rudd,[a] Andrew R. Barron,[a, f,g] and Enrico Andreoli*[a]

[a]*Energy Safety Research Institute, Swansea University, Bay Campus, Swansea, SA1 8EN, U.K.*

[b]*Department of Nuclear Engineering, Texas A&M University, College Station, TX 77843, U.S.A.*

[c]*Madrid Institute for Advanced Studies in Nanoscience, IMDEA Nanociencia, Calle Faraday 9, Ciudad Universitaria de Cantoblanco, 28049, Madrid, Spain.*

[d]*College of Engineering, Swansea University, Bay Campus, Swansea, SA1 8EN, UK.*

[e]*Materials Characterization Facility, Texas A&M University, College Station, TX 77843, U.S.A.*

[f]*Department of Chemistry, Rice University, Houston, Texas 77005, U.S.A.*

[g]*Faculty of Engineering, Universiti Teknologi Brunei, Brunei Darussalam.*

E-mail: saeid.khodabakhshi@swansea.ac.uk & E.Andreoli@Swansea.ac.uk

Abstract

Micrometer long multilayer carbon nanoribbons with high oxygen content and nitrogen doping were obtained from the nitric acid treatment of Black Pearls 2000. The nanoribbons exhibited yellow light emission under UV excitation. The oxidation of other grades of carbon black yielded irregular and small graphene oxide fragments or carbon quantum dots instead. Remarkably, the familiar and straightforward treatment of carbon materials with nitric acid reemerges as a powerful tool for the synthesis of technology-relevant carbon nanoribbons, unlocking the potential of such simple oxidation chemistry applied to cheap and commercially available carbon black.

Keywords: Carbon black, Black Pearls 2000, graphene oxide nanoribbons, UV-vis emission, nitrogen doping

1. Introduction

Carbon black (CB) is the most abundantly produced nanostructured carbon material, widely used as a conductive filler, pigment, and reinforcing agent in plastics and tire industries [1]. CB has also been investigated as an additive in composite materials for energy conversion and storage, and carbon capture [2]. One less explored use for CB, however, has been that of a precursor for carbon nanomaterials.

Similarly to graphite, CB grades such as acetylene black, furnace black and others can be oxidized in $KMnO_4$-H_2SO_4 solutions [3] or HNO_3 and HNO_3-H_2SO_4 mixtures [4-6], and subsequently exfoliated into graphene oxide (GO) [3] or graphene quantum dots (GQD) and oxidized CB particles [3, 5, 6]. Microwave-assisted oxidation of CB in an HNO_3-H_2SO_4 mixture yielded GQDs with 10 nm edge size and 2 nm thick [4]. Oxidation of Vulcan (XC-72R) with HNO_3 also yielded GQD[7, 8]. Also, CB can be converted to hollow carbon nanospheres with stacked graphene wall structure via HNO_3 oxidation at 100 °C for 96 h followed by reduction in aqueous hydrazine 100 °C for 36 h [9].

This fragmentation into different materials is possible because of the stacked graphene-like domains forming part of the basic structural unit (BSU) of CB, which also contains amorphous carbon [10]. The ratios of ordered and disordered carbon in the BSU vary among CB grades. To date, oxidation studies focused mostly on acetylene black and furnace black. These grades of CB are broadly defined by the production process, all having broad primary particle size (PPS) 15 to 40 nm in diameter and low specific surface areas (SSAs), typically less than 70 m^2/g [2]. With such a variety of nanomaterials from CB oxidation, a study on the correlation between CB grade (PPS & SSA) and resulting oxidation products (nanocarbons) is needed. The present work is focused on the effect of the oxidation of Black Pearls 2000, here labelled CB-P, in HNO_3 at 90 ^oC for 120 h, followed by centrifugation (see Supplementary Information, SI, for details).

CB-P is a high structure CB that has an average particle size of approximately 15 nm and surface area of 1500 m^2/g. These properties make CB-P an interesting starting material, as oxidation can proceed to a larger extent and deliver higher yields of exfoliated nanosheets [2]. Herein, we demonstrate that different than all low surface area CB grades tested, CB-P oxidative peeling resulted primarily in nanoribbons (NRs) with surface composition resembling that of graphene oxide. To the best of our knowledge, this is the

first time that NR morphology is obtained from CB as a precursor. Moreover, carbon quantum dots that are 2 to 10nm in size and 1nm in stacking height have more tailorable bandgaps and emissions. Changes in synthesis conditions and precurosrs dictate the particle size and functionalization. Increase in edge length of GQDs by 1nm increment and particle size distribution widths lead to aqueous suspensions with distinct emissions [11]. Changing the GQD layer thickness in light emitting devices (LEDs) [12] resulted in distinct emissions of blue and different white colors. For yellow emitting GQDs, emission shift to red or blue by dispersing these particles in polyethyleneimine (PEI) low (600Da) and high (1800Da) molecular weight, respectively [13]. Interestingly, sulfur doping of electrochemically prepared GQD[14] and nitrogen doping of GQDs obtained from hydrothermal carbonization of dopamine [15] yielded yellow emitting materials. GQD/GO composites having GQD sizes of 5-10nm and stack heights of 2-4nm, yellow, green and blue emission was obtained by increasing the GO oxidation time in NH_4OH/H_2O_2 solution at 120^oC from 40min, 120min, to 270min, respectively. Sulfur doping shift the emission to red by conducting the GO oxidation in thiourea/H_2O_2 for 10min at the same temperature [16]. On the other hand, the emission of large GO particles obtained from the Hummer's method is modulated by the controlled reduction and morphology, e.g., flakes and sheets [17-19]. These observations agree with studies conducted on the visible emission of GO, which were attributed to electron-hole recombination and involving non-oxidized carbon atoms near carbon-oxygen functional groups [20]. For GO and GQD particles obtained from CB oxidation, blue light emission under UV-vis excitation is the most characteristic. In the present work, besides demonstrating that unique ribbon morphology can be obtained, the obtained NRs emit yellow light. The simplicity of the preparation method, the ribbon morphology and emission properties make these NRs materials complementary to previously reported GOs and GQDs. These properties make our NRs promising for large scale preparation and of great technological interest [21].

2. Materials and Methods

2.1. Synthesis: Briefly, 5.0 g of Black Pearl 2000 (CB-P) were placed in a round bottom flask containing 100 mL (68%) HNO_3 and stirred at 90 °C for 120 h. The mixture was cooled down and centrifuged at 5000 rpm for 20 min to separate the supernatant from the sediment. The HNO_3 was

removed from the supernatant and the resulting brown powder was further dried at 80 °C overnight. The yield of material recovered from the supernatant (~3.3 g) was estimated as 60%. Similarly, other grades of CB were investigated, namely, Vulcan XC-72R (CB-X), Vulcan 3 (CB-V), Monarch 1000 (CB-M), and Acetylene Black (CB-A). The latter were oxidized by the same procedure and reactant amounts, except that HNO_3, was then removed by evaporation under vacuum. These CB grades have surface areas in the range of 50 to 400 m^2/g, as summarized in Table S1.

2.2. Characterization: Scanning transmission electron microscopy (STEM) and high-resolution transmission electron microscopy (HRTEM) images of the spheres were performed using a FEI Talos F200X Transmission Electron Microscope at 200 kV. Energy dispersive X-ray spectroscopy (EDS) was conducted on a carbon grid. The Raman data of the carbon spheres were recorded at room temperature using a Renishaw inVia Raman Microscope (Renishaw plc, Miskin, Pontyclun, UK) with excitation wavelength of 514 nm. The mean basal plan diameter (La), was estimated using the Raman ID/IG ratio at 514 nm laser according to the equation obtained from synchrotron X-ray scattering and from STEM [22]:

$$L_a(\text{nm}) = (2.4 \times 10^{-10})\lambda_l^4 \left(\frac{I_D}{I_G}\right)^{-1}$$

The samples were characterized using a Thermo Scientific Nicolet iS10 FT-IR Spectrometer. UV-vis spectra were measured using the Cary 300 between 800 nm and 190 nm wavelength using standard 10 mm cuvettes. Baseline was corrected to the solvent (water). The Tauc plot was calculated using the absorption coefficient (α) using the relationship between the absorption (A), the path length ($l = 1$ cm) according to $A = \alpha c l$ and the energy $\alpha = hc/\lambda$, with c being the speed of light in cm/s and λ the radiation wavelength. Powder X-ray diffraction (PXRD) patterns were collected in the 1-60° 2θ range with a Bruker D8 Avance diffractometer using Cu $K_{\alpha 1}$ radiation (λ = 1.54060 Å).

X-ray photoelectron spectroscopy (XPS) was performed using a Kratos Axis Supra (Kratos Analytical, Japan) utilizing a monochromatic Al-K_α X-ray source (K_α 1486.58 eV), 15 mA emission current, magnetic hybrid lens, and slot aperture. Region scans were performed using a pass energy of 40 eV and step size of 0.1 eV. Peak fitting of the narrow region spectra was performed using a Shirley type background, and the synthetic peaks were of a mixed Gaussian-

Lorentzian type. Carbon sp^2 was used for charge reference assumed to have a binding energy of 284 eV.

Atom Force Microscopy (AFM) was done using the Dimension Icon AFM from Bruker Corporation in tapping image mode and in ambient environment. The probe tip used was from MicroMasch, model HQ:NSC35/AL BS. The resonance frequency used was 150KHz, with scanning rate set at 1Hz. Sample per line was set at 512. The powder sample (tip of spatula) was dispersed in DI water with sonication and drop cast onto fresh cleaved Mica substrate. This was dried at ambient conditions. An aliquot of this suspension was dilute in DI water to obtain a translucent and clear suspension, which was then drop cast onto a different freshly cleaved Mica substrate and dried at the same ambient conditions.

3. Results

The oxidative peeling of CB-P yielded a product that was easily redispersed in water. Part of the product was identified by scanning transmission electron microscopy (STEM) and transmission electron microscopy (TEM) as carbon nanoribbons (NRs). These NRs were about 30 nm wide and with lengths ranging from less than 100 nm to >1500 nm. The NRs, shown in the STEM image of Fig. 1A and TEM image of Fig. 1B are formed from stacks of rectangular graphene layers. The TEM images in Fig. S1 (see SI) corroborate the NR structure is formed by the layering of rectangular graphenes.

The fast Fourier transform (FFT) electron pattern of the NR, see inset in Fig. 1A, indicates that the NRs have some degree of stacking periodicity. The d_{002}-spacing from Fast Fourier Transform (FFT) was 0.355 nm. This spacing is notably greater than for graphite, 0.3345 nm, and also larger than the value reported for unzipped multiwalled carbon nanotubes of 0.34 nm [23]. Differences would be expected given the presence of structural defects in the starting BSUs of CB, and for the introduction of heteroatoms from the oxidation of CB[2].

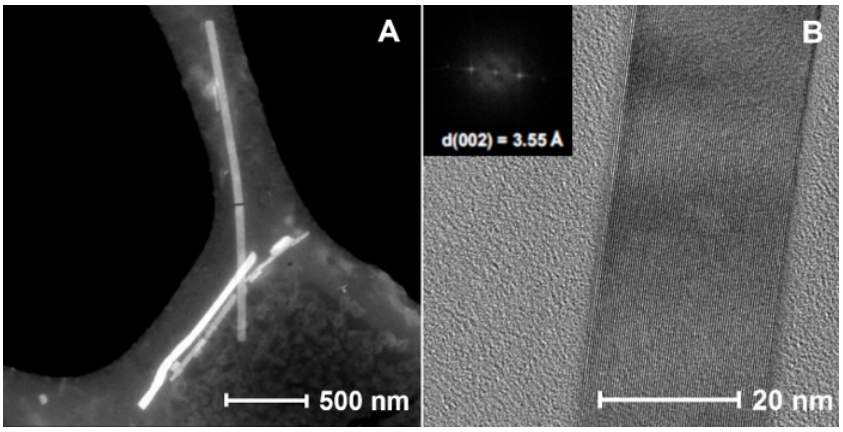

Fig. 1 – (A) STEM image of nanoribbons obtained from oxidation of CB-P in HNO_3; (B) TEM image of a nanoribbon with SAED and calculated d_{002}-spacing from FFT analysis (inset); a full version of this image with close-ups is provided in Fig. S1 (see SI).

Smaller fragments composed of squares and rectangular-shaped carbon sheets were also observed in the oxidation products of CB-P (Fig. S2). The edge lengths of the latter are comparable to the thickness of the shortest NRs, but lower magnification STEM images indicate that NRs are the predominant morphology.

The HR-TEM image in Fig. 2A shows a cluster of graphene fragments. The rectangular features are clearly visible for most of these fragments, and in agreement with low magnification STEM images of NRs. Magnification of the highlighted zone (Fig. 2B) indicated by the red circle further confirms lattice fringes of graphene material. Moreover, according to these images, as in the large are seen in Fig. 2C, most graphene fragments are composed of stacked multilayers, and individual edge structure cannot be resolved. Some regions contain single layer fragments, see Fig. 2D, but further studies are necessary to isolate and fully characterize those fragments for edge structure, composition and for in-plane defects.

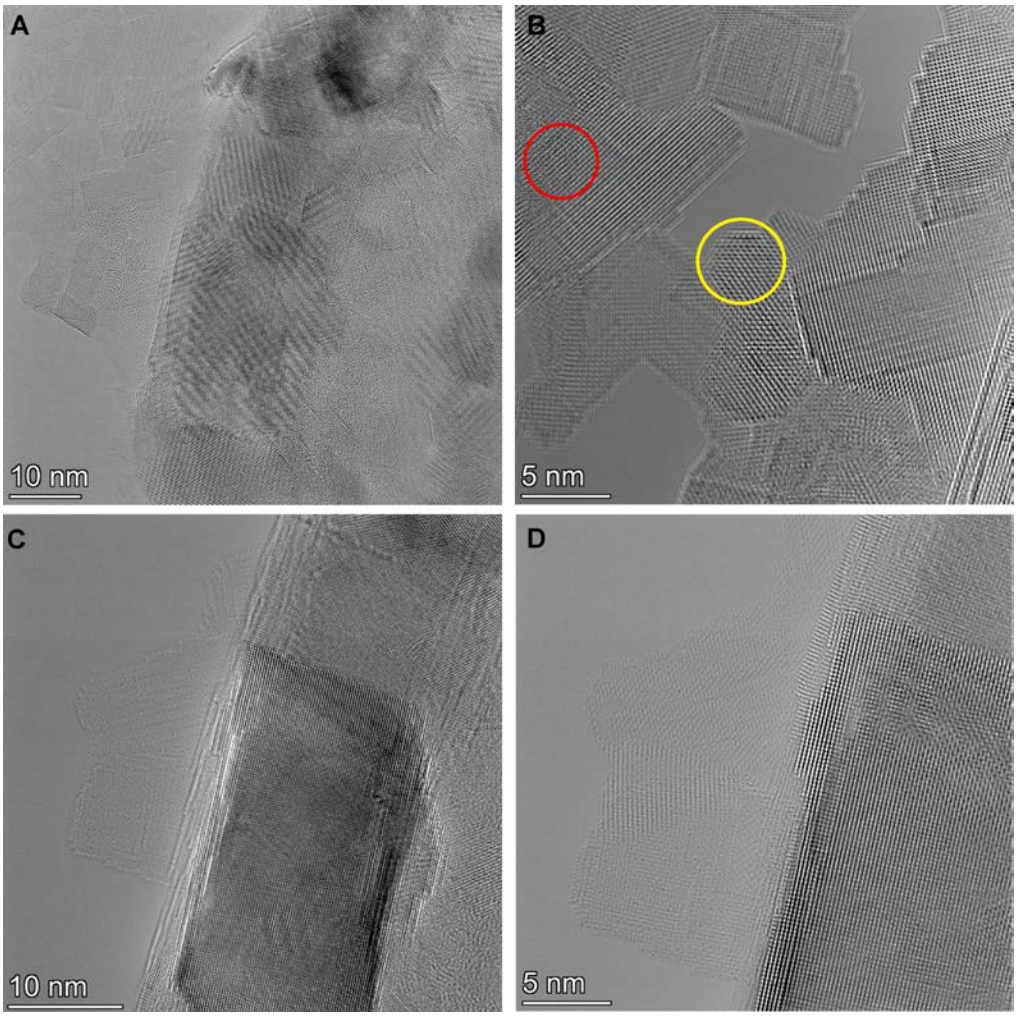

Fig. 2 – TEM Bright Field image taken from the edge of a clustered graphene sample (A). HR-TEM image taken from the thinner marked with red circle and honeycomb lattice of carbon atoms with yellow circles (B). HR-TEM image of large area rectangular fragments composed of multiplayer graphene structure (C) and magnification of edge area showing regions containing single layer graphene material (D).

CB-P was compared to other CB grades. As seen in Fig. S3, Vulcan XC-72R (CB-X) yielded agglomerates of GQDs, in agreement with previous reports [7, 8]. Interestingly, the oxidation of the another Vulcan grade, Vulcan 3 (CB-V), led to larger oxidized graphene fragments. In the case of Monarch 1000 (CB-M), a very poor yield of small fragments was obtained, which is likely due to the higher oxidation stability of this carbon black grade [2]. CB-M oxidation products had a broader distribution of particles <40 nm in size. Among the various grades of CB, Acetylene Black (CB-A) has the lowest SSA and large PPS of

67 m^2/g and 30 nm, respectively. These properties can restrict access of oxidizers to the BSUs. CB-X and CB-V have SSAs of 254 to 285 m^2/g, respectively. The average PPS for CB-X (20-50 nm) is considerably larger than for CB-V (11-19 nm). Interestingly, CB-V oxidation led to larger and more continuous graphene fragments than CB-X. This may be attributed to larger BSUs in the former than in the latter. Finally, the highest surface areas (1500 m^2/g) and 15 nm PPS of CB-P resulted in greater oxidation of the BSUs and their fragmentation into NRs, and other square and rectangular sheets. Besides accessibility, the BSUs of CB-P must contain subunit fragments with a morphology resembling the oxidation reaction products. For lower SSA CBs, higher content of amorphous carbons (primarily containing sp^3 C) may fill the voids between BSUs within each particle, as in CB-A. The presence of higher amounts of sp^3 C and more cross-linked domains further explains the lowest recovered yield of oxidized products, <10 wt.% of the starting CB-A. Indeed, previous studies have reported on the difficulty of oxidizing CB-A [6, 24], which required 200 h to 1000 h in HNO_3 to yield oxidized carbon fragments having high surface areas [6]. The poor structural ordering of the BSUs further contributes to the low oxidation yields. In general, for CB having d_{002}-spacings < 0.35 nm, the longer the time in HNO_3, the greater the extent of fragmentation for most CBs. For furnace black, with d_{002} exceeding 0.36 nm, oxidation leads to a decrease in surface area after oxidation [6]. Thus, lower amorphous carbon contents result in a higher volume of internal deep micropores, and consequently to the very high SSA of CB-P. While deep micropores are expected for Vulcan and Monarch, textural mesopores in particle aggregates are mainly responsible for their SSA. So, the yields of oxidized product from CB-V and CB-X were less than that of CB-P. As additional evidence for the transformation of the CB-P product into NR, comparison of the low magnification SEM images of the particles is provided in Fig. S4. These images show the increased surface roughness for CB-P precursor versus the particles for the layered NR product. The lack of residual particles resembling the starting CB-P and of other distinct particle morphologies corroborate with the evidence that only NR material is separated from the supernatant after oxidation, and that any residual impurities are successfully separated by centrifugation.

The Raman spectrum for NR at a laser wavelength of 514 nm (Fig. S5A, see SI) has the expected peaks near 1360 cm^{-1} and 1600 cm^{-1}, attributed to the D and G bands, respectively.

The D band is often attributed to in-plane hexagonal lattice defects. These defects lead to a turbostratic carbon structure and include heteroatoms, such as O and N, and additionally sp^3 C. The G band arises from asymmetric stretching modes of sp^2 C, as in an ordered hexagonal graphene lattice. The intensity ratio I_D/I_G for NR was approximately 0.9, which is comparable to that reported for graphene oxide and GQDs [25-27]. This ratio greatly differs from that of graphene NRs prepared by plasma etching of carbon nanotubes, and to graphenes obtained from solvent exfoliation of graphite. Both types of graphene from graphitic precursors have a far higher degree of hexagonal lattice ordering and fewer edge defects [23, 28]. In fact, the Raman spectrum of the present NRs more closely resembles that of GO prepared by oxidation of graphite. For GO, the I_D/I_G ratio further increases upon reduction to reduced graphene oxide (rGO), due to further disruption of the sp^2 C lattice [29]. Hence, the present Raman results suggest that heteroatoms are disrupting the 2D hexagonal lattice ordering within the NR basal planes [29]. Accordingly, O and N appear uniformly distributed over the NR and smaller 2D fragments, as seen in the EDX maps of Fig. 3. Most of the O and N originate from the HNO_3 [2].

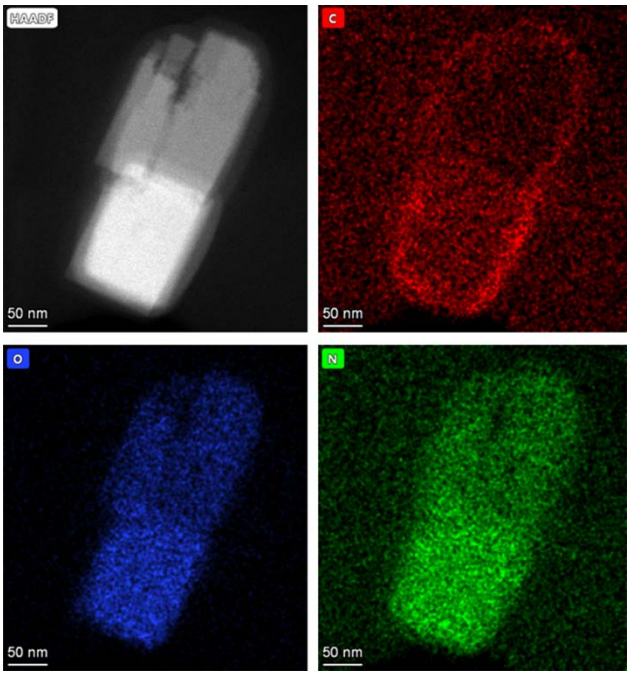

Fig. 3 – High-angle annular dark-field (HAADF) STEM image of graphene materials from CB-P oxidation (top left). Corresponding EDX mapping for C (top right), O (bottom left) and N (bottom right). Additional signals originate from the TEM grid and residual solvent used in preparing the grids.

The HAADF STEM image and the concentration of elements changing in the EDX mapping in Fig. 3 suggest the possible changes in thickness along the individual NR fragments. This was verified by AFM images which are presented in Fig. 4 for samples cast from a dilute suspension, and in Fig. S5 for those cast from a more concentrated one. Along the width of an individual NR fragment, as indicated in Fig. 4A and 4B, the thinnest region had a heinght of approximately 1.7nm. This corresponds to roughly bilayer GO assuming the 0.355nm interplanar spacing, which agrees with the thickness of monolayer GO estimated as 0.7nm [29]. According to analysis of the 3D AFM image in Fig. 4C, at its maximum height, this thickness reached roughly 8.1nm. This indicated that the NRs have step defects. The resulting structures have micron size lengths with thicknesses ranging from bilayers to nearly 12 layers. Thicker films are formed by large agglomerates containing NRs, see Fig. S6A and S6B, and regions with thicknesses of ca. 6nm are still indentified. Thus, NR particles can be reversibly separated and agglomerated.

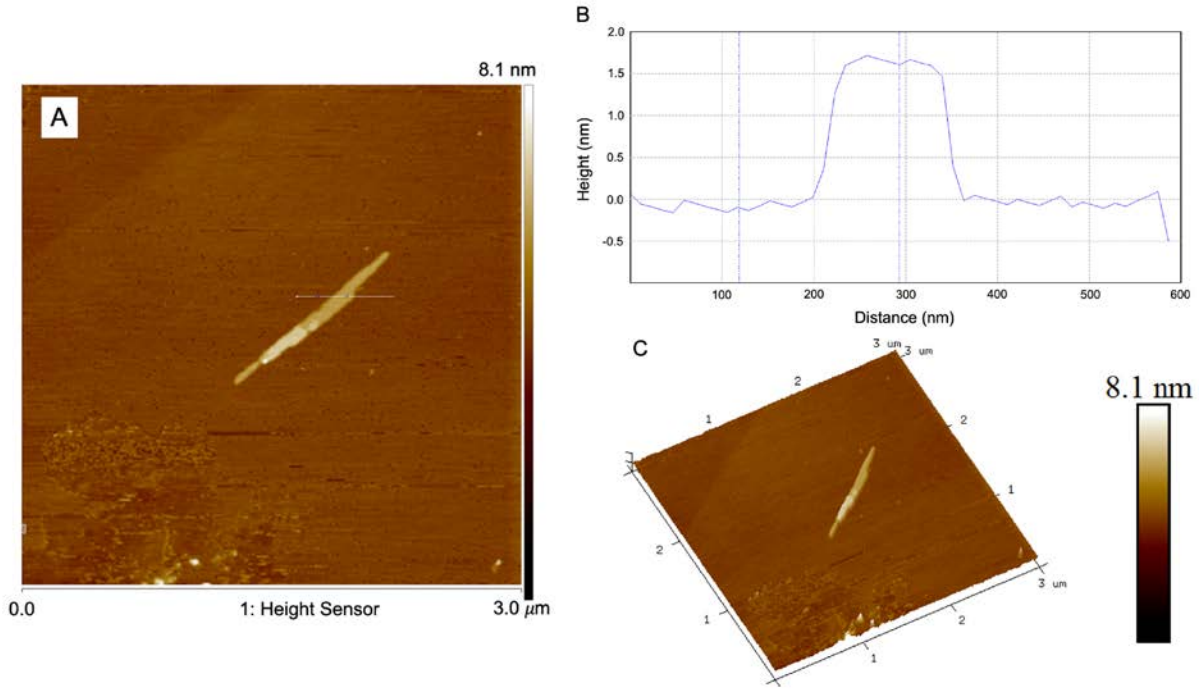

Fig. 4 – (A) 2D AFM image of NR on Mica; (B) with height profile along indicated line; (C) 3D AFM image of the same NR fragment indicating the heinght variation along the ribbon particle.

The powder XRD in Fig. S6C has a strong reflection at 21.8°. The calculated *d*-spacing was 0.407nm, which is larger than that from FFT. While the XRD pattern reflects the different products obtained within a large sample, including smaller fragments and more oxidized particles, the FFT pattern is for a single NR fragment. The peak position agrees with previously reported XRD data on mellitic acid prepared by the electrochemical oxidation of graphite in water [30]. The apparent *d*-spacing of NRs, however, agrees with that for graphite oxide of approximately 0.44 nm [31]. The mean crystallite stacking height L_c was estimated according to a modified Scherrer equation, as proposed by Knox et al. [32], with a geometry constant of 0.84. A value of L_c = 7.55 nm was thus obtained. The mean basal plane diameter, L_a = 18.6 nm, was estimated using the Raman I_D/I_G ratio at 514 nm. This differs with the typical value of L_a = 4.7 nm for GO prepared from graphite oxidation using a modified Hummer's method [33]. The present value indicates the large size of the polycrystalline domains within the turbostratic structure, and it is in agreement with HRTEM image results. These values indicate the small size of the polycrystalline domains within the turbostratic structure. The estimated L_c value also agrees with the maximum thickness height for the NR from AFM analysis. The L_c further indicates that the average is skewed towards thicker layered GO segments. Although the XRD results agree with those of graphite oxide, the existence of strongly adsorbed fragments resembling mellitic acid on the NR particles must be considered. The mellitic acid structure results from extended oxidation in HNO_3. In Fig. S6D (see SI), the FT-IR spectrum of NRs shows the presence of a significant number of C=O groups, most likely of carboxylic acid at 1698 cm^{-1}. The broad stretching absorption at 2400-3500 cm^{-1} confirms the presence of acidic OH and phenolic OH in the NRs. The peaks with low intensity at 1357 cm^{-1} and 1553 cm^{-1} suggest the presence of NO_2 groups which were already reported in the HNO_3 oxidation of CB [2].

The presence of soluble fragments resembling mellitic acid on the NRs was further confirmed by solution NMR in both deuterated methanol (MeOD) and deuterated dimethyl sulfoxide (DMSO-d_6) (Figs. S7 and S8, see SI). Carbon signals related to structures resembling that of mellitic acid (C=O at δ = 167 and C=C at δ = 133) were well-resolved in the ^{13}C-NMR of NRs in MeOD and DMSO-d_6. The ^{1}H-NMR in both MeOD and DMSO-d_6 contained sharp singlet peaks in the aromatic region (δ = 6.75-9), corresponding to phenolic OH. The acid OH signals are missing in DMSO-d_6, because of rapid proton exchange with water traces present in DMSO-d_6, thus leading to a broad signal centred at

δ = 4.5 (Fig. S7A, see SI). ^{1}H-NMR in MeOD discloses a wide range of proton environments with different multiplicity, making their assignment complex. These protons, in general, can be related to phenolic and aliphatic protons (δ = 4.75-5.25) that connect to either O or C, such as protons from aliphatic OH or connected to sp^2 carbons (δ = 5.75-6.5), aromatic protons (δ = 7-9), and phenolic and acidic OH in the most unshielded species (δ = 10-13).

The X-ray photoelectron spectroscopy (XPS) analyses of NRs (Table S2, see SI) indicated large amounts of O, and some N doping (1.5 at%). The C/O atomic ratio was approximately 2.4, a value higher than that of GO with C/O 0.7-1.2.[34] In fact, it approaches that of some rGO materials obtained using $NaBH_4$ or N_2H_2, for which C/O ranges from 2.8 to 6.2 [34]. The high-resolution XPS spectra of NRs revealed the nature of the different C, O and N surface functional groups (Fig. S5B-D, see SI). The C1s spectrum is asymmetric, which is characteristic of materials with a dominant sp^2 carbon component. A mixed Doniach Sunjic/Gaussian-Lorentzian fitting was used to model the sp^2 carbon following literature precedent with the sp^2 peak set to 284.4 eV [35, 36]. The amount of sp^2 C was much greater than that of sp^3 C, despite the high oxygen contents. The oxygenated carbon species in NRs were predominantly carbonyl and carboxylic acid functional groups. This is reflected in the size of the deconvoluted XPS C1s at 288.8 and 289.2 eV, respectively (Fig. S5D). Moreover, in the C1s spectrum, the signal corresponding to the C-N bond overlapped with the C-OH and C-O-C signals, meaning that it was not possible to obtain a specific peak location corresponding to C-N. The N1s spectrum reveals N in three different environments. The main N1s peak was assigned to quinoline-/graphitic-type nitrogen, concurring with previous observations [37, 38]. Oxidised N was also present as N-O and NO_2 at 400.5 and 405.0 eV, respectively. The O1s spectrum supports the C1s spectrum, with peaks corresponding to C-OH and O=C-O present at 532.7 and 531.5 eV, respectively. The O=C-O peak dominates the region where N-O would be expected, and this is due to the relatively small quantity of nitrogen present in the sample [39].

Recent studies using HR STEM have shown that continuous carbon films cover entire lines of CB particles. These films follow the individual CB particle curvature [40]. Various CB grades prepared by different methods and precursors, namely channel, furnace, lamp and thermal black have different degrees of particle aggregation. The thermal black

materials have been found to have lower degree of aggregation and better uniformity of the individual CB nanoparticles [40]. CB-P and Vulcan grades are prepared by the furnace black process, and these have more uniform structures and are less agglomerated than CB-A which is an acetylene black type of material. As aforementioned, the major differences among CB-P and Vulcan materials are on the surface area, amount of amorphous carbon blocking pores formed by the BSUs [2]. Also the length of the fringes forming BSUs and their tortuosity vary among furnace black grades [40]. Moreover, TEM images of CB-P (BP-2000) and of CB-V grade (Vulcan XC-72R) in Fig. S9, reveal that CB-P is formed by particle agglomerates with fewer CBs along the aggregate width, and that these grow preferentially in a one-dimensional fashion. CB-V, however, is formed of larger agglomerates that extend over two-dimensional areas.

Considering the structural information on the NRs, a possible mechanism for the formation of these nanostructures from CBs, which are composed of aggregates of spherical nanoparticles having graphene and turbostratic carbon domains is proposed. The continuous carbon film connecting the agglomerate of primary particles of CB-P provide the building block for large NR fragments. In the present study, we collected evidence that these films, which are peeled off during oxidation in HNO_3, have a multilayer graphene structure and with oxygen and nitrogen functional groups. Since most of these graphene fragments extend over all interconnected particles, NRs that separate during oxidation have lengths corresponding to a single CB or to an extended one-dimensional line of primary particle agglomerates. The width is controlled by that of graphene over the fewer interconnected CBs particles. With these long ribbons, smaller fragments peel off simultaneously and stack up over the largest ones. The smaller fragments correspond to smaller lines of CB particles and even to the size of graphene particles forming the BSUs of individual CB particles. Consequently, a variety of lengths for the ribbons are obtained, while having very consistent widths. Whereas, graphene films that are peeled off from the Vulcan grades, CB-X and CB-V, investigated by HNO_3 oxidation method have less defined shapes and size.

Finally, the ultraviolet-visible (UV-vis) absorption spectrum of the NRs exhibits an absorption band at 288 nm, Fig. 5A. The absorption spectrum differs from that of mellitic acid, which is narrow and has two fine overlapping absorption peaks near 300 nm. Evidence

of the bathochromic effect is also observed, the broad absorption at wavelengths greater than 300 nm is typical of the presence of polyaromatic structures where a large number aromatic rings merge to form an extended sp^2 system [41, 42].

Using 365 nm lamp irradiation, a solution of NRs in water emitted yellow luminescence, Fig. 5B, which is different from Vulcan XC-72R oxidation products [7]. The visible bandgap was estimated using the Tauc plot (see Fig. S10, SI), lying in the range of 3.2-3.9 eV. Previously reported large GO and rGO fragments with similar C/O ratios to the present NRs had bandgaps of 4.0-4.5 eV. The latter materials exhibited blue emission, thus exceeding the energy for blue light (2.5-2.75 eV). Excitation and electron-hole recombination in discrete states within the band structure of small domains are responsible for the blue emission [20, 43].

Other N-doped GO materials had valence band-maximum (VBM) from valence-band photoemission spectroscopy (VB-PES), or Fermi level, estimated at 3.1 eV for 2.7 at.% N, which in turn was mostly pyrrolic. Increasing the N content to 5.0 at% further lowered the VBM to 2.6 eV due to N-lone-pair electrons, π-electrons of C-N bonds and σ-electrons of C-N bonds with increasing N content. Pure GO had a VBM of 5.1 eV, whereas the VBM for highly oriented pyrolytic graphite (HOPG) was 1.8 eV [44]. Moreover, the longer wavelength yellow emission of the present NRs agrees with an investigation on N-doped GQDs, for which the emission changed from blue to green and then to yellow by systematically increasing the extent of the graphene π-system conjugation [45]. These results provide additional support for an extended π-system and the impact of N-doping (quinoline/graphitic, -NO and $-NO_2$) in the properties of the materials.

The photoluminescence (PL) and PL Excitation (PLE) spectra of NRs recorded in a spectrofluorimeter (FluoroMax-4 TCSPC Horiba Jobin Yvon) by using a 1 cm standard quartz cuvette. Fig. 5C represents the PL and PLE of NRs dissolved in isopropyl alcohol (IPA) solvent. PLE spectrum of NRs displays a band with a peak at 510 nm (black line, Fig. 5C). Meanwhile, the PL spectrum upon 490 nm photoexcitation is characterized by a broad band with a maximum at 560 nm (blue line, Fig. 5C) which is in line with the yellow color emission under the UV light irradiation, Fig. 5B. It is worth mentioning that, the PL spectra were photoexcited by different wavelengths, showing similar PL characteristics that are centred at 560 nm.

For comparison, the PL and PLE of sample mellitic acid, CB-M and CB-C were measured in proper solvents. The sample of mellitic acid was dissolved in H_2O with heating, whereas the oxidation products from CB-M and of CB-V were dispersed in isopropyl alcohol (IPA) and in chloroform($CHCl_3$) respectively.

In Fig. 5D, the PL excitation of mellitic acid (black line) is composed of band with vibrionic progressions at 357, 370 and 395 nm and a PL emission band (red line) that is centered at 431 nm. The PLE and PL spectra of oxidized CB-M has a broad excitation band at 597 nm, as seen in Fig. 5E, (black line). The PL spectrum photoexcited at 570 nm depicts a broad band with maximum at 670 nm (red line). The PLE spectrum of sample obtained from CB-V, see black line in Fig. 5F, is characterized by a band at 455 nm along with a peak at 324 and a shoulder 377 nm. The PL spectra upon 325 nm photoexcitation (blue line) and 450nm (red line) are composed of a peak at ~537 nm.

Based on the drastic differences in optical properties, it can be concluded that all the samples are different from the NRs. While mellitic acid has blue emission, CB-M and CB-V have red and yellow emissions, respectively. These differences can be related particles size, new electron transitions caused by N-doping and in addition to those from aromatic C domains near C-O functional groups, and by hybrid electronic and vibrionic states [20, 43, 45]. Similar to NRs, the CB-V materials were composed of large N-doped GO sheet structure. These differ from CB-M that was composed of smaller fragments, and that were obtained in small yield. Compared to all materials, the photoluminescence properties of the NRs and its unique morphology are of great interest in sensing and bioimaging, as components in display and solar energy conversion devices, and as photocatalysts [45-48].

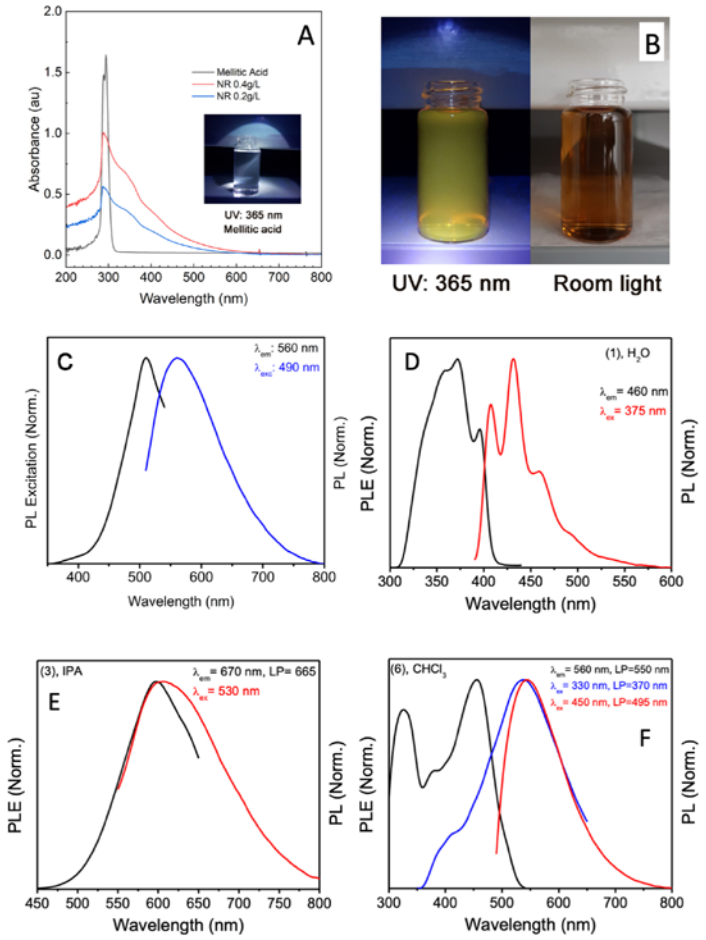

Fig. 5 – (A) UV-vis absorption spectra of mellitic acid and NRs in water (red line: 0.4 g/L and blue line: 0.2 g/L), and a digital photograph of an aqueous mellitic acid solution under UV light (inset). (B) Digital photographs of NR aqueous suspension under 365 nm UV radiation (left) and under ambient light (right). (C) PL (blue line, λexc=490 nm) and PL excitation (blackline, λ_{em}=560 nm) spectra of NRs measured in IPA. (D) PLE (λ_{em}= 460 nm) and PL (λ_{exc}= 375 nm) spectra of sample 1 (Mellitic acid) dissolved in H_2O with heating. (E) PLE (λ_{em}= 670 nm) and PL (λ_{exc}= 530 nm) spectra of CB-M dispersed in IPA. Long pass (LP) filter was used sometimes in order to remove the scattering. (F) PLE (λ_{em}= 560 nm) and PL (λ_{exc}= 330 and 450 nm) spectra of CB-V dispersed in $CHCl_3$.

4. Conclusion

In summary, a facile method for obtaining carbon nanoribbons from the oxidation of carbon black Black Pearl 2000 in HNO_3 is reported. Other grades of CB materials yielded graphene

quantum dots, most likely due to differences in the BSUs of the materials investigated. The NR graphene stackings were approximately 30 nm thick with lengths reaching several microns. The NRs have a turbostratic carbon structure, with high oxygen content between the values reported for graphene oxide and reduced graphene oxide materials. Smaller oxygen-rich fractions resembling mellitic acid were found on the oxidized surfaces, but the overall properties of NRs differed significantly from those of mellitic acid, as confirmed by SAED, Raman and UV-vis spectroscopy. Results point to the synergistic effect of the local extended π-systems and the N-doping resulting in the yellow emission properties of the NRs.

Acknowledgement

S. K. wishes to acknowledge funding from the European Union's Horizon 2020 research and innovation programme under the Marie Skłodowska-Curie grant agreement No 663830. Financial support was also provided by the Reducing Industrial Carbon Emissions (RICE) operation part-funded by the EU's European Regional Development Fund through the Welsh Government. The authors also acknowledge the assistance provided by the Swansea University AIM Facility, funded in part by the EPSRC (EP/M028267/1), the European Regional Development Fund through the Welsh Government (80708) and the Sêr Solar project via the Welsh Government. Use of the TAMU Materials Characterization Facility and Dr. Wilson Serem are acknowledged.

Supplementary Information

Supplementary Material available CB and NR materials properties, elemental composition, STEM, XPS, XRD, FTIR, ^{1}H and ^{13}C NMR, Tauc plot) at DOI:

References

[1] Carbon, 6. Carbon Black, Ullmann's Encyclopedia of Industrial Chemistry.

[2] S. Khodabakhshi, P.F. Fulvio, E. Andreoli, Carbon black reborn: Structure and chemistry for renewable energy harnessing, Carbon 162 (2020) 604-649.

[3] P.M. Wilson, F. Orange, M.J.F. Guinel, M. Shekhirev, Y. Gao, J.A. Colon Santana, A.A. Gusev, P.A. Dowben, Y. Lu, A. Sinitskii, Oxidative peeling of carbon black nanoparticles, RSC Advances 5(112) (2015) 92539-92544.

[4] C.-C. Wang, S.-Y. Lu, Carbon black-derived graphene quantum dots composited with carbon aerogel as a highly efficient and stable reduction catalyst for the iodide/tri-iodide couple, Nanoscale 7(3) (2015) 1209-1215.

[5] P. Xue, J. Gao, Y. Bao, J. Wang, Q. Li, C. Wu, An analysis of microstructural variations in carbon black modified by oxidation or ultrasound, Carbon 49(10) (2011) 3346-3355.

[6] K. Kamegawa, K. Nishikubo, H. Yoshida, Oxidative degradation of carbon blacks with nitric acid (I)—Changes in pore and crystallographic structures, Carbon 36(4) (1998) 433-441.

[7] Y. Dong, C. Chen, X. Zheng, L. Gao, Z. Cui, H. Yang, C. Guo, Y. Chi, C.M. Li, One-step and high yield simultaneous preparation of single- and multi-layer graphene quantum dots from CX-72 carbon black, J. Mater. Chem. 22(18) (2012) 8764-8766.

[8] L. Chen, C.X. Guo, Q. Zhang, Y. Lei, J. Xie, S. Ee, G. Guai, Q. Song, C.M. Li, Graphene Quantum-Dot-Doped Polypyrrole Counter Electrode for High-Performance Dye-Sensitized Solar Cells, ACS Applied Materials & Interfaces 5(6) (2013) 2047-2052.

[9] J. Wutthiprom, N. Phattharasupakun, M. Sawangphruk, Turning Carbon Black to Hollow Carbon Nanospheres for Enhancing Charge Storage Capacities of LiMn2O4, LiCoO2, LiNiMnCoO2, and LiFePO4 Lithium-Ion Batteries, ACS Omega 2(7) (2017) 3730-3738.

[10] H. Marsh, F. Rodríguez-Reinoso, CHAPTER 2 - Activated Carbon (Origins), in: H. Marsh, F. Rodríguez-Reinoso (Eds.), Activated Carbon, Elsevier Science Ltd, Oxford, 2006, pp. 13-86.

[11] L. Wang, W. Li, L. Yin, Y. Liu, H. Guo, J. Lai, Y. Han, G. Li, M. Li, J. Zhang, R. Vajtai, P.M. Ajayan, M. Wu, Full-color fluorescent carbon quantum dots, Science Advances 6(40) (2020) eabb6772.

[12] L. Yin, J. Zhou, W. Li, J. Zhang, L. Wang, Yellow fluorescent graphene quantum dots as a phosphor for white tunable light-emitting diodes, RSC Advances 9(16) (2019) 9301-9307.

[13] T. Gao, X. Wang, L.-Y. Yang, H. He, X.-X. Ba, J. Zhao, F.-L. Jiang, Y. Liu, Red, Yellow, and Blue Luminescence by Graphene Quantum Dots: Syntheses, Mechanism, and Cellular Imaging, ACS Applied Materials & Interfaces 9(29) (2017) 24846-24856.

[14] S. Li, Y. Li, J. Cao, J. Zhu, L. Fan, X. Li, Sulfur-Doped Graphene Quantum Dots as a Novel Fluorescent Probe for Highly Selective and Sensitive Detection of Fe3+, Analytical Chemistry 86(20) (2014) 10201-10207.

[15] Z. Wang, D. Chen, B. Gu, B. Gao, Z. Liu, Y. Yang, Q. Guo, X. Zheng, G. Wang, Yellow emissive nitrogen-doped graphene quantum dots as a label-free fluorescent probe for Fe3+ sensing and bioimaging, Diamond and Related Materials 104 (2020) 107749.

[16] C.-C. Ke, Y.-C. Yang, W.-L. Tseng, Synthesis of Blue-, Green-, Yellow-, and Red-Emitting Graphene-Quantum-Dot-Based Nanomaterials with Excitation-Independent Emission, Particle & Particle Systems Characterization 33(3) (2016) 132-139.

[17] Z. Luo, P.M. Vora, E.J. Mele, A.T.C. Johnson, J.M. Kikkawa, Photoluminescence and band gap modulation in graphene oxide, Applied Physics Letters 94(11) (2009) 111909.

[18] C.-T. Chien, S.-S. Li, W.-J. Lai, Y.-C. Yeh, H.-A. Chen, I.-S. Chen, L.-C. Chen, K.-H. Chen, T. Nemoto, S. Isoda, M. Chen, T. Fujita, G. Eda, H. Yamaguchi, M. Chhowalla, C.-W. Chen, Tunable Photoluminescence from Graphene Oxide, Angewandte Chemie International Edition 51(27) (2012) 6662-6666.

[19] G. Xin, Y. Meng, Y. Ma, D. Ho, N. Kim, S.M. Cho, H. Chae, Tunable photoluminescence of graphene oxide from near-ultraviolet to blue, Materials Letters 74 (2012) 71-73.

[20] J. Shang, L. Ma, J. Li, W. Ai, T. Yu, G.G. Gurzadyan, The Origin of Fluorescence from Graphene Oxide, Scientific Reports 2(1) (2012) 792.

[21] R. Ma, Y. Zhou, H. Bi, M. Yang, J. Wang, Q. Liu, F. Huang, Multidimensional graphene structures and beyond: Unique properties, syntheses and applications, Prog. Mater Sci. 113 (2020) 100665.

[22] L.G. Cançado, K. Takai, T. Enoki, M. Endo, Y.A. Kim, H. Mizusaki, A. Jorio, L.N. Coelho, R. Magalhães-Paniago, M.A. Pimenta, General equation for the determination of the crystallite size La of nanographite by Raman spectroscopy, Applied Physics Letters 88(16) (2006) 163106.

[23] L.Y. Jiao, L. Zhang, X.R. Wang, G. Diankov, H.J. Dai, Narrow graphene nanoribbons from carbon nanotubes, Nature 458(7240) (2009) 877-880.

[24] G. Norwitz, M. Galan, Dissolution of carbon blacks by nitric acid, Carbon 5(3) (1967) 287-289.

[25] J.-B. Wu, M.-L. Lin, X. Cong, H.-N. Liu, P.-H. Tan, Raman spectroscopy of graphene-based materials and its applications in related devices, Chemical Society Reviews 47(5) (2018) 1822-1873.

[26] Y. Li, Y. Zhao, H. Cheng, Y. Hu, G. Shi, L. Dai, L. Qu, Nitrogen-Doped Graphene Quantum Dots with Oxygen-Rich Functional Groups, Journal of the American Chemical Society 134(1) (2012) 15-18.

[27] S. Wang, Y. Zhang, H.-L. Ma, Q. Zhang, W. Xu, J. Peng, J. Li, Z.-Z. Yu, M. Zhai, Ionic-liquid-assisted facile synthesis of silver nanoparticle-reduced graphene oxide hybrids by gamma irradiation, Carbon 55 (2013) 245-252.

[28] Y. Hernandez, V. Nicolosi, M. Lotya, F.M. Blighe, Z.Y. Sun, S. De, I.T. McGovern, B. Holland, M. Byrne, Y.K. Gun'ko, J.J. Boland, P. Niraj, G. Duesberg, S. Krishnamurthy, R. Goodhue, J. Hutchison, V. Scardaci, A.C. Ferrari, J.N. Coleman, High-yield production of graphene by liquid-phase exfoliation of graphite, Nature Nanotechnology 3(9) (2008) 563-568.

[29] S. Stankovich, D.A. Dikin, R.D. Piner, K.A. Kohlhaas, A. Kleinhammes, Y. Jia, Y. Wu, S.T. Nguyen, R.S. Ruoff, Synthesis of graphene-based nanosheets via chemical reduction of exfoliated graphite oxide, Carbon 45(7) (2007) 1558-1565.

[30] A.-L. Cui, G.-X. Feng, Y.-F. Zhao, H.-Z. Kou, H. Li, G.-H. Zhu, H.-S. Hwang, H.-C. Oh, Y.-J. Kwon, D.-C. Lee, Synthesis and separation of mellitic acid and graphite oxide colloid through electrochemical oxidation of graphite in deionized water, Electrochemistry Communications 11(2) (2009) 409-412.

[31] M.M. Hantel, T. Kaspar, R. Nesper, A. Wokaun, R. Kötz, Partially reduced graphite oxide for supercapacitor electrodes: Effect of graphene layer spacing and huge specific capacitance, Electrochemistry Communications 13(1) (2011) 90-92.

[32] J.H. Knox, B. Kaur, G.R. Millward, Structure and performance of porous graphitic carbon in liquid chromatography, Journal of Chromatography A 352 (1986) 3-25.

[33] A. Ganguly, S. Sharma, P. Papakonstantinou, J. Hamilton, Probing the Thermal Deoxygenation of Graphene Oxide Using High-Resolution In Situ X-ray-Based Spectroscopies, The Journal of Physical Chemistry C 115(34) (2011) 17009-17019.

[34] D.R. Dreyer, S. Park, C.W. Bielawski, R.S. Ruoff, The chemistry of graphene oxide, Chem. Soc. Rev. 39(1) (2010) 228-240.

[35] J.A. Rudd, D.R. Jones, C.W. Dunnill, E. Andreoli, Study of copper(II) oxide and copper(II) acetate on multiwalled carbon nanotubes by XPS, Surface Science Spectra 26(1) (2019) 014013.

[36] J. Tarábek, L. Kavan, L. Dunsch, M. Kalbac, Chemical States of Electrochemically Doped Single Wall Carbon Nanotubes As Probed by Raman Spectroelectrochemistry and ex Situ X-ray Photoelectron Spectroscopy, The Journal of Physical Chemistry C 112(36) (2008) 13856-13861.

[37] C. Zhan, X. Yu, Q. Liang, W. Liu, Y. Wang, R. Lv, Z.-H. Huang, F. Kang, Flour food waste derived activated carbon for high-performance supercapacitors, RSC Advances 6(92) (2016) 89391-89396.

[38] E. Andreoli, A.R. Barron, Correlating Carbon Dioxide Capture and Chemical Changes in Pyrolyzed Polyethylenimine-C60, Energy & Fuels 29(7) (2015) 4479-4487.

[39] N. Tawil, E. Sacher, E. Boulais, R. Mandeville, M. Meunier, X-ray Photoelectron Spectroscopic and Transmission Electron Microscopic Characterizations of Bacteriophage–Nanoparticle Complexes for Pathogen Detection, The Journal of Physical Chemistry C 117(40) (2013) 20656-20665.

[40] M. Singh, R.L. Vander Wal, Nanostructure Quantification of Carbon Blacks, C 5(1) (2019).

[41] R.N. jones, The Ultraviolet Absorption Spectra of Aromatic Hydrocarbons, Chemical Reviews 32(1) (1943) 1-46.

[42] O. Thomas, M. Brogat, Chapter 3 - Organic Constituents, in: O. Thomas, C. Burgess (Eds.), UV-Visible Spectrophotometry of Water and Wastewater (Second Edition), Elsevier2017, pp. 73-138.

[43] G. Eda, Y.-Y. Lin, C. Mattevi, H. Yamaguchi, H.-A. Chen, I.-S. Chen, C.-W. Chen, M. Chhowalla, Blue Photoluminescence from Chemically Derived Graphene Oxide, Advanced Materials 22(4) (2010) 505-509.

[44] C.-H. Chuang, S.C. Ray, D. Mazumder, S. Sharma, A. Ganguly, P. Papakonstantinou, J.-W. Chiou, H.-M. Tsai, H.-W. Shiu, C.-H. Chen, H.-J. Lin, J. Guo, W.-F. Pong, Chemical Modification

of Graphene Oxide by Nitrogenation: An X-ray Absorption and Emission Spectroscopy Study, Scientific Reports 7(1) (2017) 42235.

[45] D. Qu, M. Zheng, J. Li, Z. Xie, Z. Sun, Tailoring color emissions from N-doped graphene quantum dots for bioimaging applications, Light: Science & Applications 4(12) (2015) e364-e364.

[46] M. Li, T. Chen, J.J. Gooding, J. Liu, Review of Carbon and Graphene Quantum Dots for Sensing, ACS Sensors 4(7) (2019) 1732-1748.

[47] S.N. Baker, G.A. Baker, Luminescent Carbon Nanodots: Emergent Nanolights, Angewandte Chemie International Edition 49(38) (2010) 6726-6744.

[48] C. Han, N. Zhang, Y.-J. Xu, Structural diversity of graphene materials and their multifarious roles in heterogeneous photocatalysis, Nano Today 11(3) (2016) 351-372.